Int J Adv Manuf Technol (2017) 92:4445–4455
DOI 10.1007/s00170-017-0441-8

ORIGINAL ARTICLE

Identification of forming limit curve at fracture in incremental sheet forming

Van-Cuong Do[1] · **Quoc-Tuan Pham**[1] · **Young-Suk Kim**[2]

Received: 9 February 2017 / Accepted: 19 April 2017 / Published online: 19 May 2017

Abstract Computer-aided manufacturing technology is widely used in the sheet-forming industry to predict forming performance. Strain-based forming limit criterion is popularly used for this purpose. In incremental sheet forming, the forming limit curve at fracture (FLCF) is a line from the equi-biaxial strain-point to plane strain-point and is high in comparison with those in conventional press forming methods. This study aims to empirically define the FLCF, specifically the equi-biaxial strain at fracture which has yet to be experimentally defined. In addition, to confirm the experimental measurement results, the finite element simulation by ABAQUS/Explicit was performed wherein the fitted flow curve of the large-strain range, accompanied with non-associated flow rule yield behaviour, demonstrates good agreement with the experiment. A new stress-strain equation is thus introduced to describe the flow curve in a large-strain range.

Keywords Incremental sheet forming (ISF) · Forming limit curve at fracture · Equi-biaxial strain · Non-associated flow rule · Finite element simulation

1 Introduction

The first method of incremental sheet forming (ISF) with a single point tool, called "dieless forming," was patented by Leszak in 1967 [1]. The concept of asymmetrical incremental sheet forming (AISF) by computer numerically controlled machine was subsequently published in 1992 [2] and has dramatically improved upon as described in 2005 in the review paper [3]. The deformation mechanisms of ISF is stretching and shear in the plane perpendicular to the tool direction, with shear in the plane parallel to the tool direction. Strain components increase on successive laps, and the most significant component of strain is shear parallel to the tool direction [4].

Unlike the forming limit diagram (FLD) in conventional press forming expressed in terms of principal strain conditions for the onset of localized necking, incremental sheet forming is limited by fracture with suppression of necking [5]. The forming limit curve at fracture (FLCF) in the incremental forming process has much higher strain compared with the classical FLD and shows a straight line having a negative slope of the form $\varepsilon_1 = a\varepsilon_2 + b$ in the first quadrant. It is noted that this straight line of FLCF of sheet material is very similar to the shape of the FLC when the sheet thickness becomes nearly zero. The slope of FLCF is concluded to be about −1 [3, 6, 7].

In recent papers, authors performed many tests to define the FLCF by pyramidal shape, cone shape and compared to the values taken from bulge tests. The main conclusion is that the FCLF is independent on strain path, and the experimental slope of FCLF for 1.0-mm-thick AA1050-H111 sheet ranges from −0.7 [8] and −0.86 [9, 10]. Another suggestion is that the FLCF should be considered as mechanical properties of material instead of FLD. The different slope of FLCF comes from the different measurement methods of equi-biaxial strain at fracture.

In several recent articles [8–10], the fracture strain measured at the corner of formed pyramidal shape is far from equi-biaxial strain. A cross-arc groove tool path was subsequently introduced to perform the fracture at equi-biaxial state

✉ Young-Suk Kim
caekim@knu.ac.kr

[1] Graduate School, Kyungpook National University, Daegu 41566, Republic of Korea

[2] School of Mechanical Engineering, Kyungpook National University, Daegu 41566, Republic of Korea

with the smaller 15-mm-diameter tool [11, 12]. In this test, the fracture occurred at the outer groove terminal first, rather than the cross-groove area and the strain was measured by grid analysis with a grid size of 2 mm. However, the grid analysis can only give a correct result when the ratio of tool diameter and grid size is about 50. In addition, the 3D-DIC results showed that these points are far from the equi-biaxial strain [13]. This suggests that the equi-biaxial strain at fracture point has not yet been defined.

In this study, we introduce an apparatus to define the fracture limit line in ISF by three points: the plane strain point, the equi-biaxial strain point and in-between these two points. The measurement result is also confirmed by numerical simulation by ABAQUS/Explicit using flow curve fitted by Kim-Tuan equation and non-associated flow rule yield behaviour. The mechanical properties of 0.8-mm-thick AL5052-O sheet material are also clarified in advance.

2 Experiments

2.1 Material properties

To obtain the flow stress-strain relation for AL5052-O sheet, a series of uniaxial tensile tests were performed following the ASTM-8 standard procedure at a constant tensile speed of 20 mm/min with a gauge length of 50 mm. The laser cutting method was applied to prepare the specimens in order to increase the accuracy and reduce the effect of the cutting process on the surface of the specimens.

To evaluate the anisotropic plasticity behaviour, tensile tests were conducted in three different directions, at 0°, 45° and 90°, with respect to the rolling direction. The material properties are summarized in Table 1, including Young's modulus (E), ultimate tensile strength (UTS), and elongation (Δl). The initial yield stress and the plastic strain ratios (R *values*) are also reported respectively for the three directions (σ_0, σ_{45}, σ_{90}, R_0, R_{45}, R_{90}).

Figure 1 presents the true stress-true strain curves of the studied material for three different orientations. As noted in Table 1, the AL5052-O sheet is an anisotropic material, expressed by the differences of both the initial yield stresses and the plastic strain ratios in the three different orientations. Furthermore, from Fig. 1, it is clear that the flow curves in different directions are represented by different curvatures, which are distinct in tensile strength, elongation, and necking area.

Table 1 Mechanical properties of Al5052-O

Direction	0°	45°	90°
Young modulus (GPa)	73.2	71.2	64.1
Yield stress (MPa)	183.3	172.5	173.6
Ultimate tensile strength (MPa)	229.8	216.6	220.1
Elongation (%)	11.0	13.6	10.5
R value	0.758	0.646	0.863
K_T	131.580	124.809	124.268
m	0.271	0.278	0.251
c	61.163	75.433	69.521

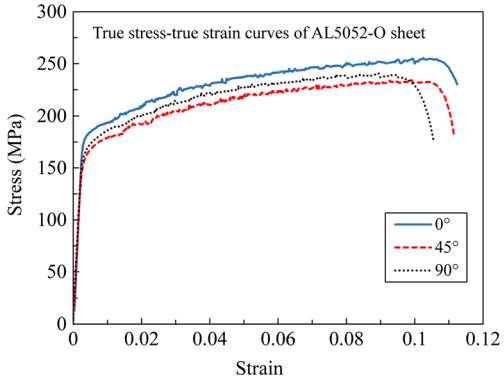

Fig. 1 Stress-strain curves of the of AL5052-O sheet for three different orientations

Conventionally, either the Swift equation (power law) or the Voce equation (exponent law) is applied to describe the strain-hardening behaviour of sheet metals. However, using these equations to predict the post-necking behaviour of sheet metals remains questionable, as indicated in the work of Coppieters [14]. Therefore, we propose a new hardening model, the Kim-Tuan model [15], to model the stress-strain relation of AL5052-O sheet material with the aim of successfully describing the material behaviour on both sides of the necking point: pre-necking behaviour and post-necking behaviour. The formulation of Kim-Tuan (K-T) hardening model is expressed as follows:

$$\sigma = \sigma_0 + K_T(\varepsilon + \varepsilon_0)^m(1-\exp^{-c\varepsilon}) \quad (1)$$

where K_T, m, and c are the parameters of the proposed equation, and m is the dependent parameter calculated by

$$m = \frac{\sigma^*}{\sigma^* - \sigma_0}\left(\varepsilon^* + \varepsilon_0\right) \quad (2)$$

where (ε_0, σ_0) is the initial yield point of the true stress-true strain curve and (ε^*, σ^*) are plastic strain and stress in accordance with maximum tensile force point. It is clear that parameter m is a dependent parameter whose value does not depend on other parameter values. Therefore, the value of parameters K_T and c in the Kim-Tuan model can be found using the curve fitting tool available on some optimization packages, such as Excel or MATLAB. The Kim-Tuan equation can be easily reduced to the Swift equation when σ_0 is ignored and c is infinity. Additionally, this equation can be simplified to the Voce equation when the value of parameter m is zero.

Figure 2 provides the curve fitting results for the AL5052-O sheets using three different strain hardening models: the Swift power law, the Voce exponent law, and the newly proposed Kim-Tuan equation. In the three models, the Kim-Tuan hardening model enforces the work-hardening rate or the slope of stress-strain curve (dσ/dε) at the maximum tensile force point of the fitted curve equal to that of the experiment. This makes the proposed equation advantageous for studying the post-necking behaviour of sheet metals without requiring any other plasticity properties, except the stress-strain data from the uniaxial tensile test.

The hydraulic bugle test was also performed to get the biaxial stress-biaxial strain (σ_b, ε_b) data as the following equation.

$$\sigma_b = \frac{pR_d}{2t_d}; \varepsilon_b = ln\left(\frac{t_d}{t_0}\right) \tag{3}$$

Therefore, biaxial stress and biaxial strain can be calculated based on three measurable variables: the hydraulic pressure p recorded by a pressure gauge, the bulge radius R_d, and the polar thickness t_d determined using ARAMIS system (see Fig. 3a).

The curve fitting result of the tensile test data in the rolling direction by Kim-Tuan equation was compared with the stress-effective strain curve obtained from the hydraulic bulge test, as shown in Fig. 3b. It is clear that the strain hardening curve obtained from the Kim-Tuan equation is well matched with the experimental data from the bulge test in all ranges of strain. As such, the Kim-Tuan equation provides an accurate prediction for the post-necking behaviour of the AL5052-O sheets. It is, thus, reasonable to conclude that the strain hardening function based on the Kim-Tuan equation can be applied in the simulation process, as discussed in the next section.

2.2 Forming limit curve at fracture in incremental sheet forming

To define the FLCF, we performed experiments to measure strain value at three points: the plane strain point, the equi-biaxial strain point and in-between these two points. Truncated pyramidal shapes with square base of 80 × 80 mm were formed to find the limited forming angle and plain strain at fracture. In these tests, we employed the z-level tool path as Fig. 4. The other forming parameters include a tool diameter of 10 mm, vertical step of 0.4 mm, feed rate of 800 mm/min, spindle speed of 60 round/min and MoS2 lubrication.

The maximum forming angle can be achieved at 64° and fracture occurs at 65° of wall angle for 0.8-mm-thick AL5052-O material. Laser cutting was applied to cut the cross section along the wall of pyramidal parts. The thickness distribution along the wall of pyramids are measured as indicated in

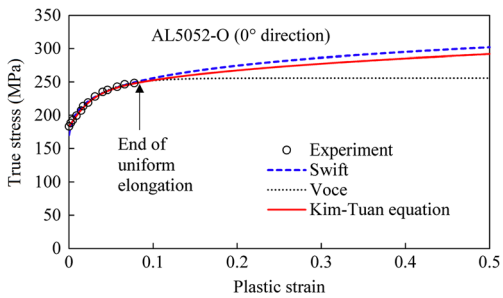

Fig. 2 Curve fitting results for the AL5052-O sheet in the rolling direction

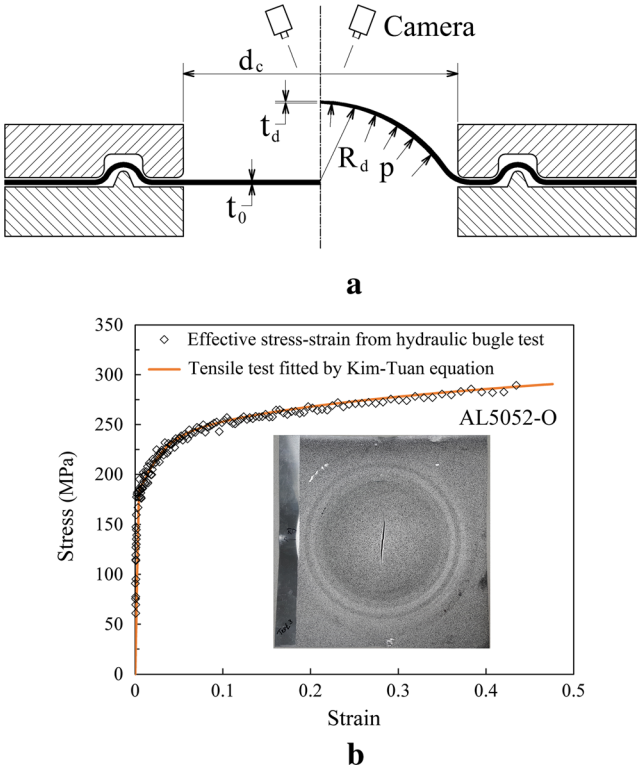

Fig. 3 **a** Hydraulic bulge test set up. **b** Comparison of the results of the Kim-Tuan hardening function and the effective stress-strain data from the hydraulic bulge test for the AL5052-O sheet material

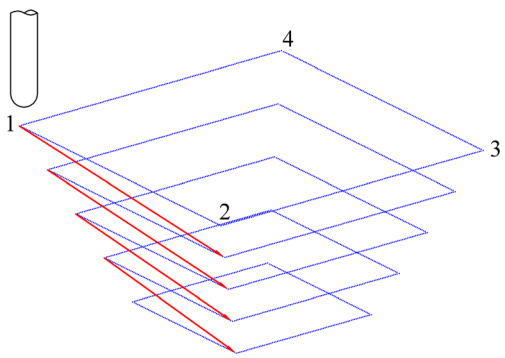

Fig. 4 Tool path used for pyramidal part

Fig. 5a. Figure 5b shows the minimum thickness locating at the forming depth of 7 ÷ 11 mm, this value is significantly lower than the value calculated by cosine law. The minimum thickness for the safe part of 64° and fracture part of 65° are 0.245 and 0.224 mm, respectively. The thickness strain is calculated, and this magnitude value is considered as major strain because the pyramid wall can be considered to deform in plane strain mode [16].

To perform equi-biaxial strain deformation, we introduced a new tool path named four-wing-star. This new tool path is performed for AL5052-O first and tested for some industrial materials such as stainless steel STS 304, mild steel, and pure titanium. The experiments were done for tool diameter of 10 mm. Before the test, 0.2-mm-pitch grids are marked to roughly define the major and minor deformations.

The forming setup and tool path are shown in Fig. 6a, b. The specimen with the size of 140 × 140 mm is clamped on the plus-shape die. The plus-shape die is cut from chemical wood in order to support the blank shoulder. The points named A, B, C and D are located at the plane higher than the initial sheet plane where the tool is not in contact with the sheet metal. The tool moves in order of 1–2–3–4–5–6–7–8 with downward distance of ΔZ in the centre area, and it is repeated with a depth increment ΔZ of 0.25 mm.

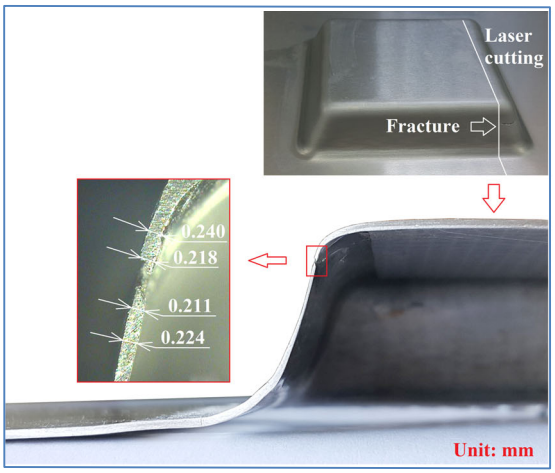

Fig. 5 **a** Microscopic thickness measurement of pyramidal shape of 65° (thickness at area close to fracture). **b** Thickness distribution of the wall in pyramidal shape

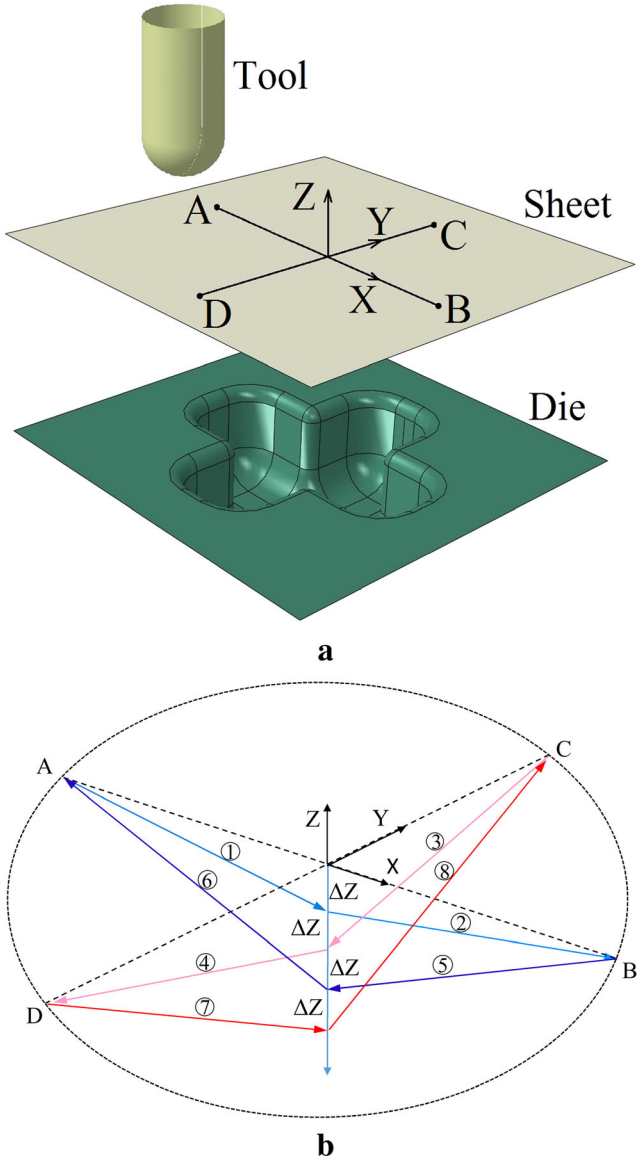

Fig. 6 **a** Forming set up for defining equi-biaxial strain. **b** Four-wing-star tool path for equi-biaxial strain evolution

When the tool continuously descends to the centre position, fracture occurs at this area as shown in Fig. 7. In all experiments, the fracture occurred in the centre area first and the tests were stopped immediately. The grid marking shows that the centre area is in an equi-biaxial strain state. Thus, the thickness strain magnitude is double value of major and minor strain.

With the same measurement method, the minimum thickness distribution along the cross section was measured. For AL5052-O specimen, the minimum thickness close to fracture

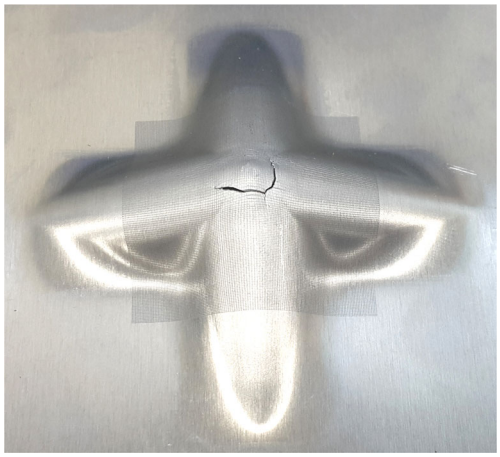

Fig. 7 Fracture at the centre area of the four-wing star specimen (bottom view)

point is measured as 0.235 mm, approximately to the case of the 65-degree pyramidal part. The thickness distribution along the symmetric cross section is shown as Fig. 13 in the next section.

Another tool path named two-wing star as a part of the four-wing star tool path was introduced to define the fracture locating between plane strain point and equi-biaxial point. In this tool path, the tool moves from A to B and repeats with downward distance of ΔZ in the centre area as Fig. 8a. After the fracture occurred as shown in Fig. 8b, the grid analysis method with grid size of 0.2 mm was used to measure the strain pair around the fracture position. The strain evolution was further clarified in the next section by numerical simulation also.

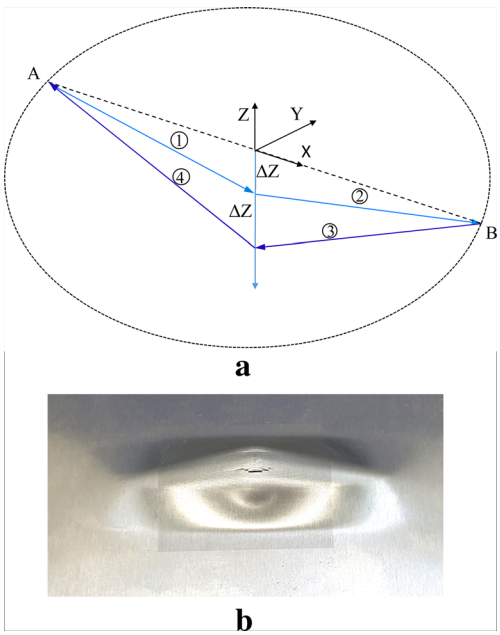

Fig. 8 **a** Two-wing-star tool path. **b** Fracture happens for the two-wing-star tool path

The major and minor strain at fracture boundary between the safety and failure zone is plotted in Fig. 9. The fitted FLCF for AL5052-O material is as follows:

$$\varepsilon_1 = -1.04\varepsilon_2 + 1.24 \quad (4)$$

where ε_1 and ε_2 are the major and minor strains, respectively.

The same tool path was applied for some other industrial materials with different tensile strength such as soft material (Al3000-O), high strength material (STS304) and hard-to-form material (pure titanium), as Fig. 9b–d.

To verify again the strain deformation for the new tool paths, the numerical simulation was performed to clarify the major and minor strain evolution. Thickness distribution was also taken into consideration.

3 Finite element simulation

3.1 The non-associated flow rule with mixed hardening

The ISF is a slow process with cyclic and local plastic strain. The finite element simulation is a great challenge. The main challenge is to simulate thousands of increments along the long forming time with small element in the small contact area. The plastic deformation occurs around the tool contact area while the rest of the area is under elastic deformation. To describe the material behaviour, combined isotropic/ nonlinear kinematic hardening model showed the effectiveness [16, 17]. Another challenge is to accurately describe the material flow curve up to large-strain range. As shown in the previous section, the Kim-Tuan hardening equation is the best for fitting the stress-strain curve in a post-necking range. Regarding the integration strategy, many studies performed the simulation by implicit and explicit solutions. The implicit analysis gives favourable results compared to experiments in the case of geometry and springback, but long computational time is a drawback [3, 18]. On the other hand, the explicit solution is using mass scaling and time scaling, which reduces the simulation time and offers good accuracy [19].

In this study, AL5052-O sheet was used. It is undeniable that AL5052-O is an anisotropic material due to both the mean of tensile strength and the anisotropic plastic ratio [20]. From this point of view, anisotropic functions should be used to derive the plastic work behaviour of this material. Thus, in this study, we considered two approaches in the field of plasticity to describe the plastic work behaviours of the studied material: the associated flow rule (AFR) and the non-associated flow (NAFR).

In the first approach of associated flow rule, the material's plastic work behaviours involved the plasticity yield function and the plasticity potential function are described by only one

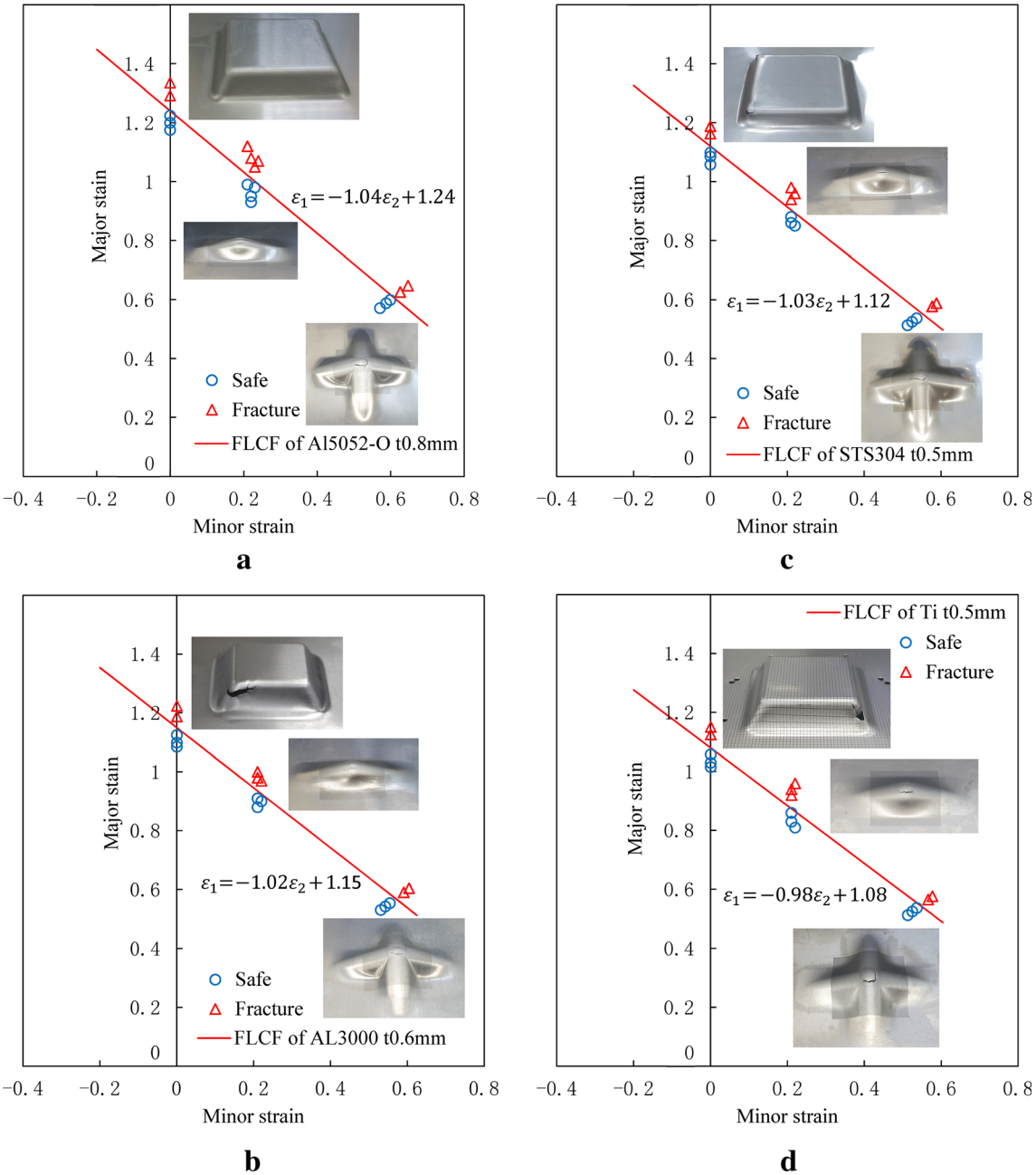

Fig. 9 **a** FLCF of 0.8-mm-thick AL5052-O. **b** FLCF of 0.6-mm-thick AL3000. **c** FLCF of 0.5-mm-thick STS304. **d** FLCF of 0.5-mm-thick pure titanium

function. For aluminium sheet metals, especially for AL5052-O sheet, YLD2000-2D yield function has been proven as the most accuracy yield function. In the other approach, non-associated flow rule, the most important point is that the plastic yield function and the plastic potential function are expressed by two different functions. It is more complicated when these two functions are formulated by different mathematical forms. Therefore, to simplify the calculation process, both plastic yield function and plastic potential function are expressed in the form of Hill's quadratic formulation [17]. However, the value of parameters of the yield function (F, G, H, N) were calculated based on the stress terms (σ_0, σ_{45}, σ_{90}, and σ_b) while the value of parameters of potential function (F', G', H', N') were determined based on strain terms (R_0, R_{45}, R_{90}). Further formulation of the Hill's quadratic function can be found in reference. The parameters of these functions are reported in Table 2.

The yield criterion, as function of all state variables, can be written in a generic form as

$$F\left(\sigma, \alpha, \sigma^Y\right) = f_y(\sigma - \alpha) - \sigma^Y(p) = 0 \tag{5}$$

Table 2 Parameters of material AL5052-O

Yield function Hill48-σ			
F	G	H	N
0.5144	0.3995	0.6005	1.8012
Potential function Hill48-R			
F'	G'	H'	N'
0.4996	0.5688	0.4312	1.2244

where $f_y(\sigma-\alpha)$ is a continuously differentiable yield function; α is a backstress tensor in the kinematic hardening model, and if α is ignored, the yield criterion returns to isotropic hardening model; p is the equivalent plastic strain; $\sigma^Y(p)$ is the work hardening rule which is generally represented by Swift, Voce or Kim-Tuan equation.

The evolution of the backstress tensor is modelled based on the nonlinear kinematic hardening theory of the so-called Armstrong-Frederick model (AF model):

$$d\alpha = \left(\frac{C}{f_p}\eta - \gamma\alpha\right)dp \tag{6}$$

in which tensor η is defined as $\eta = (\sigma-\alpha)$; C *and* γ are material constants. For tested AL5052-O material, C *and* γ are taken the values of 1118.26 MPa and 23.694, respectively.

Hill 1948 anisotropic yield function in the plane stress condition:

$$f_y = \frac{1}{2}\sqrt{(G+H)\eta_x^2 + (F+H)\eta_y^2 - 2H\eta_x\eta_y + 2N\eta_{xy}^2} - \frac{1}{2} = 0 \tag{7}$$

σ^Y is the yield stress in the reference direction and F, G, H and N are constant characteristics of the anisotropy and are defined as:

$$\begin{aligned} 2G &= \frac{1}{\left(\sigma_0^Y\right)^2} - \frac{1}{\left(\sigma_{90}^Y\right)^2} + \frac{1}{\left(\sigma_B^Y\right)^2}; \\ 2F &= \frac{1}{\left(\sigma_0^Y\right)^2} + \frac{1}{\left(\sigma_{90}^Y\right)^2} - \frac{1}{\left(\sigma_B^Y\right)^2}; \\ 2H &= \frac{1}{\left(\sigma_0^Y\right)^2} + \frac{1}{\left(\sigma_{90}^Y\right)^2} - \frac{1}{\left(\sigma_B^Y\right)^2}; \\ 2N &= \frac{1}{\left(\sigma_{\text{shear}}^Y\right)^2} = \frac{4}{\left(\sigma_{45}^Y\right)^2} - \frac{1}{\left(\sigma_B^Y\right)^2} \end{aligned} \tag{8}$$

where σ_0^Y, σ_{90}^Y, and σ_{45}^Y are tensile yield stresses in the rolling, transverse and diagonal directions, σ_{shear}^Y is the shear yield stress and σ_B^Y is the equi-biaxial yield stress.

The plastic potential function can be defined in the form of Hill 1948 anisotropic function as follows:

$$f_p = \sqrt{(G'+H')\eta_x^2 + (F'+H')\eta_y^2 - 2H'\eta_x\eta_y + 2N'\eta_{xy}^2} \tag{9}$$

In which the set of anisotropic coefficient, F′, G′, H′ and N′ are functions of the plastic strain ratios defined as follows:

$$\begin{aligned} G' &= \frac{1}{1+R_0}; H' = \frac{R_0}{1+R_0}; F' = \frac{R_0}{(1+R_0)R_{90}}; \\ N' &= \frac{(1+2R_{45})(R_0+R_{90})}{2(1+R_0)R_{90}} \end{aligned} \tag{10}$$

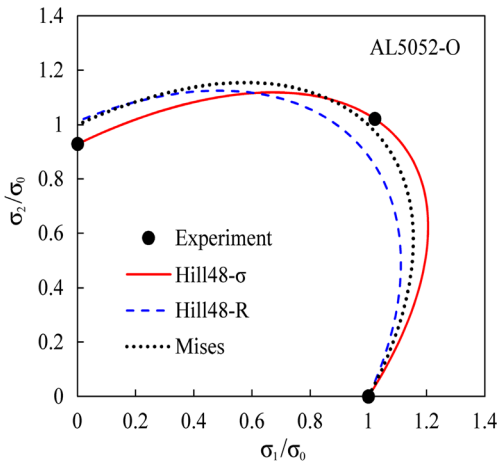

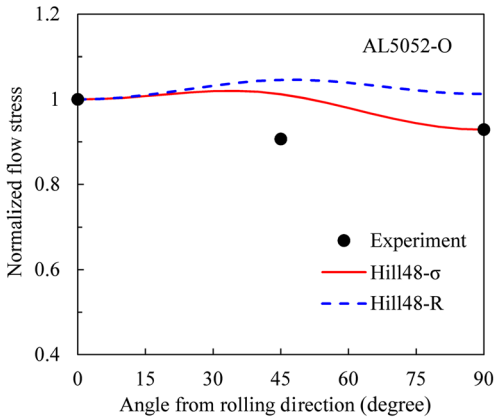

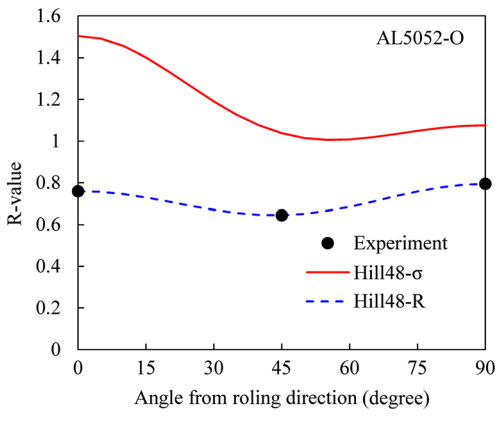

Fig. 10 **a** Comparison of plastic work behaviours of the AL5052-O sheets based on different approaches. **b** Normalized yield flow stress predicted by different yield functions and experimental data. **c** R value predicted by different potential function and experimental data

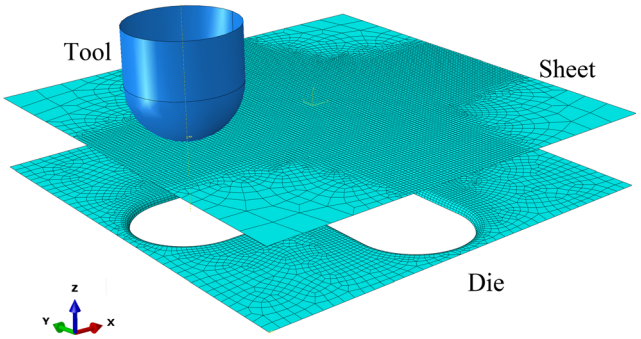

Fig. 11 FEM model for four-wing stars tool path

Figure 10a shows a comparison of the plastic work behaviours of the AL5052-O sheet based on two approaches: the non-associated flow rule with Hill's quadratic function (labelled "Hill48-σ" for yield function and "Hill48-R" for potential function). Additionally, experimental data of yield loci of AL5052-O obtained from uniaxial tensile tests and bulge test are compared in this figure.

It is clear that the Hill48-σ yield function successfully describe the yielding behaviour of the selected material. Both of these functions predict the experimental data of yield stress obtained from the uniaxial tensile tests and bulge test. However, the notable difference between the two functions was seen at the plane strain mode. Furthermore, in NAFR approach, the yield function and the potential function are represented by two significantly different curvatures. It is remarkable that these functions are represented by only one curvature in the AFR approach.

Additionally, comparisons between predicted anisotropy and experimental data of AL5052-O sheet are shown in Fig. 10b, c. The applications of the Hill48-σ to predict normalized yield stress and the Hill48-R to describe R value at different orientations are in agreement with the experiment data. However, using Hill48-σ to predict R value or applying Hill48-R to predict normalized yield stress leads to a significantly discrepant result with experiment data. The ability of NAFR approach with Hill's quadratic formulation on

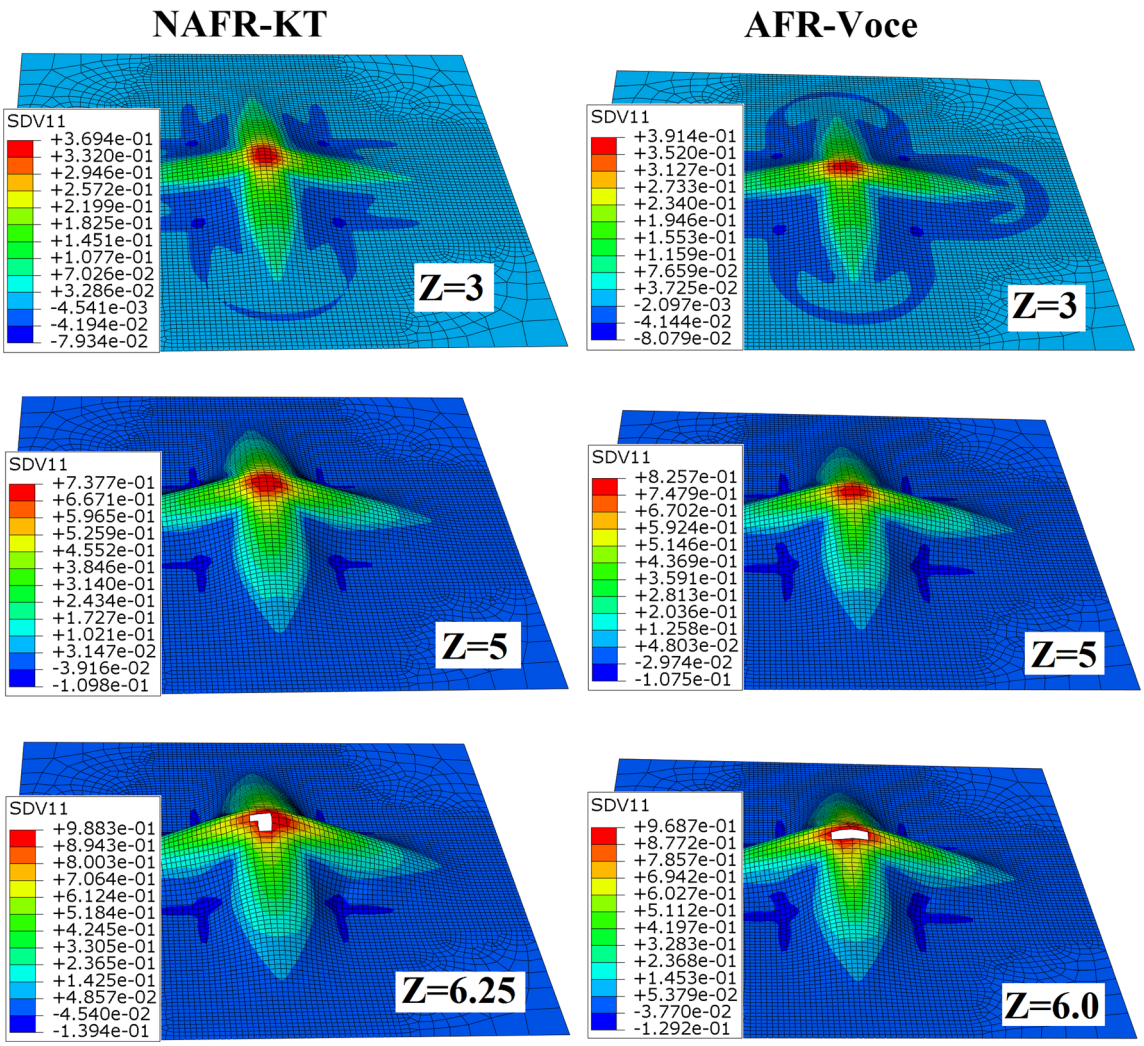

Fig. 12 Fracture variable state (*SDV11*) comparison

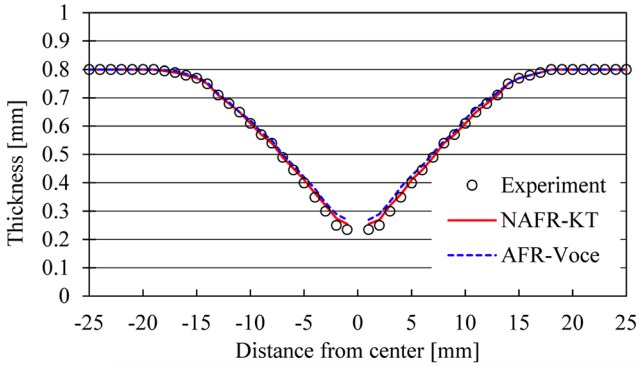

Fig. 13 Thickness distribution along the cross section

describing the plastic work behaviour of AL5052-O sheet material is confirmed.

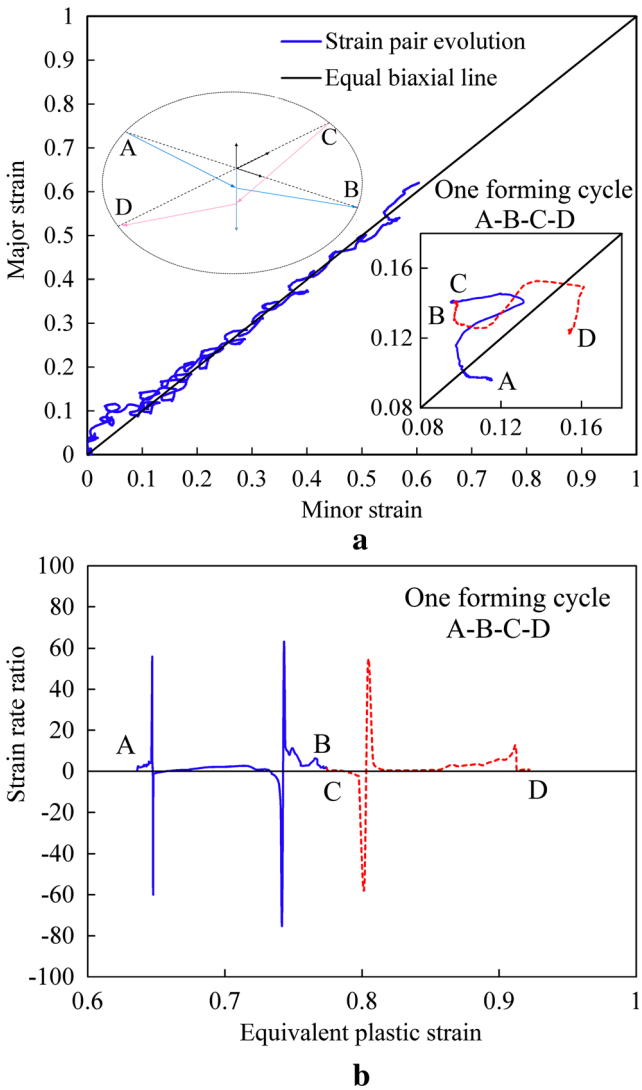

Fig. 14 **a** Major and minor strain evolution of deleted element in case of NAFR-KT model. **b** Strain rate ratio subjected to equivalent plastic strain for one forming cycle

3.2 FEM model

The software ABAQUS version 6.14 is used for elastic-plastic simulations of incremental forming process for defining equi-biaxial strain described in the previous section.

The finite element model is shown in Fig. 11. The full model is considered to ensure the correct results because the symmetry condition does not correctly describe the mechanical deformation of the sheet during forming process. The AL5052-O sheet is meshed by square shape, S4R type with a size of 0.5 mm, and is integrated by Gauss integration with 9 points in through-thickness direction. The outer boundary of the sheet is constrained by 6° of freedom. The fixed die is modelled as discrete rigid body and meshed by the R3D4 element. The tool with a diameter of 10 mm is modelled as analytically rigid.

A VUMAT subroutine was developed accompanying with flow curve of Kim-Tuan equation and NAFR Hill48 yield function (NAFR-KT case) in the simulation of the four-wing star test for the AL5052-O sheet. Other material models by AFR and flow curve fitted by Voce equation (AFR-Voce) was performed to compare the simulation prediction.

Additionally, the forming limit diagram criterion (FLDCRT) is applied to predict the fracture phenomena during the forming process [10, 11]. The FLCF for material Al5052-O is described by the equation $\varepsilon_1 = -1.04\varepsilon_2 + 1.24$. In simulation, the fracture is considered to occur at one element when its FLDCRT value, which is defined by the ratio of the major strains (ε_{1Cal}) and the FLC values (ε_{1FLCF}) at the same point for the minor strains (ε_2), reaches to the unit value.

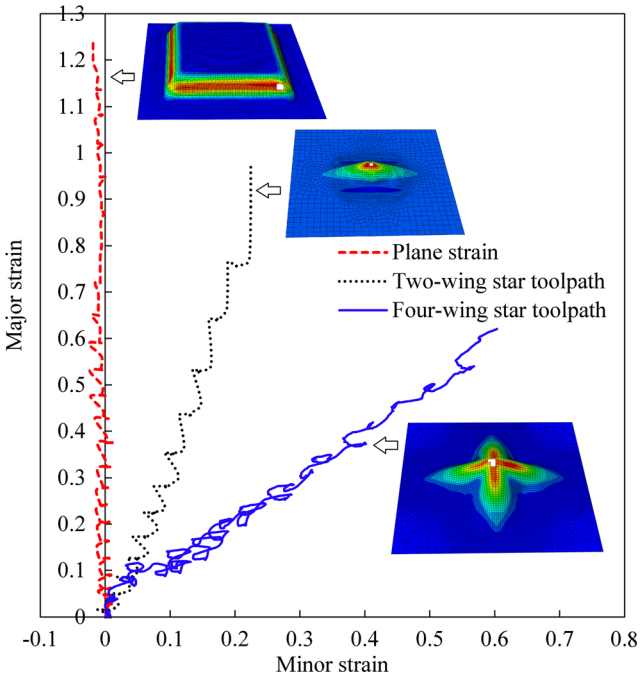

Fig. 15 Strain evolution for the deleted elements in the simulation

In this simulation, the FLDCRT value at elements in the centre area is over the unit first, the elements are deleted (Fig. 12).

Figure 12 shows the FLDCRT value (*SDV11*) evolution for NAFR-KT and AFR-Voce. In both cases, this value is always the maximum in the centre area during the forming process. Notable, however, the FLDCRT values for AFR-Voce case are always higher than those in NAFR-KT case and the fracture depth predictions are 6.25 and 6.0 mm for NAFR-KT and AFR-Voce model, respectively, in comparison with 6.50 mm in the experiment.

When the fracture occurred, thickness in the cross section is measured for both AFR-Voce and NAFR-KT model (Fig. 13). The thickness around the fracture area in NAFR-KT and AFR-Voce models are 0.245 and 0.264 mm, respectively, compared with 0.235 mm in the experiment. The thickness evolution shows that in the small plastic strain area, the predictions by AFR-Voce and NAFR-KT models are similar to the experiment results. However, in the large plastic strain area (near centre area), the NAFR-KT model gives the better result in comparison with AFR-Voce model. The thickness distribution gets the minimum value at the centre area (distance from centre of about 3 mm). In this area, the thickness can be considered to be homogenous.

The major and minor strain evolution for deleted element in the centre area was plotted with the equi-biaxial line (major strain = minor strain) (Fig. 14a). In this figure, the strain pair evolution for one forming cycle in which the tool goes in the order A–B–C–D as shown in Fig. 6b was magnified. When the tool goes from A to B, the major strain tends to increase faster than the minor strain and the element changes from compression to tension. The trend is similar when the tool goes from C to D with faster increment of the minor strain. The strain rate ratio changes the sign repeatedly as shown in Fig.14b. The process is repeated for many forming cycle. The strain evolution is not absolutely equi-biaxial stretching but the general trend deviates slightly from it.

The same simulation schemes were applied to simulate the 65-degree pyramid part and two-wing star tool path to predict the fracture and the strain evolution for deleted elements for each shape, as plotted in Fig. 15. This shows that the element in the wall of pyramidal shape can be considered as plane strain deformation. For the case of four-wing star tool path, the strain pair ratio deviated lightly from the equal stretching line. Finally, the strain evolution for the deleted elements in the two-wing star tool path is in-between the plane strain and equi-biaxial strain. This predicted fracture point is in good agreement with the grid analysis result.

4 Conclusions

In this paper, we shortly summarized the basic concept of, briefly synthesized literature on, FLCF. In addition, we developed a new method and the associated apparatus to define FLCF, especially the equi-biaxial strain point at fracture. By the four-wing-star tool path, the centre area is deformed as the equi-biaxial strain state and reached to fracture first. By two-wing-star tool path, the strain evolution is in-between plane strain and equi-biaxial strain.

From this experimental works for some industrial material with different yield strengths and crystal structures, the slope of FLCF is defined about minus unit.

In the numerical simulation, the Kim-Tuan equation offered the best fitting result for stress-strain curve at large-strain range because the hardening rate at the maximum tensile force point is taken into consideration. In addition, the NAFR accompanied with the Hill 1948 yield function and Kim-Tuan hardening equation is applied in simulation to accurately predict the fracture occurrence as well as thickness distribution.

Acknowledgements This work was supported by the National Research Foundation of Korea (NRF) grant funded by the Korean government (MEST) (No.2014R1A2A2A01005903).

References

1. Leszak E (1967) Aparatus and process for incremental dieless forming. United States Patent Office 3342051A1
2. Iseki H, Kato K, Sakamoto S (1992) Flexible and incremental metal bulging using a path-controlled spherical roller. Trans Japan Soc Mech Engng 58(554):3147–3155
3. Jeswiet J, Micari F, Hirt G, Bramley A, Duflou J, Allwood J (2005) Asymmetric single point incremental forming of sheet metal. CIRP Annals-Manuf Technol 54(2):88–114
4. Jackson K, Allwood J (2009) The mechanics of incremental sheet forming. J Mater Proc Technol 209:1158–1174
5. Seong DY, Haque MZ, Kim JB, Stoughton TB, Yoon JW (2014) Suppresion of necking in incremental sheet forming. Int J Solids and Struct 51:2840–2849
6. Jeswiet J, Young D (2005) Forming limit diagrams for single-point incremental forming of aluminum sheet. J Eng Manuf 219(4):359–364
7. Silva MB, Skjoedt M, Martins PAF, Bay N (2008) Revisiting the fundamentals of single point incremental forming by means of membrane analysis. Int J Machine Tool Manuf 48:73–83
8. Isik K, Silva MB, Tekkaya AE, Martins PAF (2014) Formability limits by fracture in sheet metal forming. J Mater Proc Technol 214: 1557–1565
9. Soeiro JMC, Silva CMA, Silva MB, Martins PAF (2015) Revisiting the formability limits by fracture in sheet metal forming. J Mat Proc Technol 217:184–192
10. Silva MB, Isik K, Tekkaya AE, Martins PAF (2015) Fracture loci in sheet metal forming: a review. Acta Metall Sin 28(12):1415–1425
11. Filice L, Fantini L, Micari F (2002) Analysis of material formability in incremental forming. CIRP Ann - Manuf Technol 51(1):199–202
12. Wang J, Li L, Wang B, Jiang H (2013) Study on formability of TRIP steel in incremental sheet forming. Adv Mater Res 634: 2881–2884
13. Decultot N, Robert L, Velay V, Bernhart G (2010) Single point incremental sheet forming investigated by in-process 3D digital image correlation. EPJ Web Conf 6:11001

14. Coppieters S, Kuwabara T (2014) Identification of post-necking hardening phenomena in ductile sheet metal. Exp Mech 54:1355–1371
15. Pham QT, Kim YS (2016) Evaluation of press formability of pure titanium sheets. Key Eng Mater 716:87–98
16. Nguyen DT, Park JG, Kim YS (2010) Ductile fracture prediction in rotational forming for magnesium alloy sheets using combined kinematic/isotropic hardening model. Metall Mater Trans A 41A: 1983–1994
17. Taherizadeh A, Green DE, Ghaei A, Whan YJ (2010) A non-associated constitutive model with mixed iso-kinematic hardening for finite element simulation of sheet metal forming. Int J Plast 26: 288–309
18. Ambrogio G, Filice L, Gagliardi F, Micari F (2005) Sheet thinning prediction in single point incremental forming. Adv Mater Res 6:479–486
19. Bambach M, Ames J, Azaouzi M, Compagne L, Hirt G, Batoz J L (2005) Initial experimental and numerical investigations into a class of new strategies for single point incremental sheet forming (SPIF). The 8th int ESAFORM conf Mat Form:671–674
20. Tamura S, Sumikawa S, Uemori T, Hamasaki H, Yoshida F (2011) Experimental observation of elasto-plasticity behavior of type 5000 and 6000 aluminum alloy sheets. Mater Trans 52(5):868–875